ARTICLE

doi:10.1038/nature25152

Mean global ocean temperatures during the last glacial transition

Bernhard Bereiter[1,2,3], Sarah Shackleton[1], Daniel Baggenstos[1,2], Kenji Kawamura[4,5,6] & Jeff Severinghaus[1]

Little is known about the ocean temperature's long-term response to climate perturbations owing to limited observations and a lack of robust reconstructions. Although most of the anthropogenic heat added to the climate system has been taken up by the ocean up until now, its role in a century and beyond is uncertain. Here, using noble gases trapped in ice cores, we show that the mean global ocean temperature increased by 2.57 ± 0.24 degrees Celsius over the last glacial transition (20,000 to 10,000 years ago). Our reconstruction provides unprecedented precision and temporal resolution for the integrated global ocean, in contrast to the depth-, region-, organism- and season-specific estimates provided by other methods. We find that the mean global ocean temperature is closely correlated with Antarctic temperature and has no lead or lag with atmospheric CO_2, thereby confirming the important role of Southern Hemisphere climate in global climate trends. We also reveal an enigmatic 700-year warming during the early Younger Dryas period (about 12,000 years ago) that surpasses estimates of modern ocean heat uptake.

Today, the global ocean takes up about 93% of the excess heat from anthropogenic activities[1], which dominates the current global radiation imbalance[2]. Owing to the heterogeneity and size of the global ocean it is difficult to measure its heat content and mean (global) ocean temperature (MOT) precisely. A large number of sensors are needed to track regional changes and derive global trends, as in the Argo float array project[3]. Nevertheless, this system does not yet cover much of the deep ocean (depth below 2,000 m), leaving uncertainty in the MOT estimates for the current warming. For changes in MOT before the Argo float system started (around AD 2,000), the data basis is much weaker, because the observations were much more sparse[1]. Considering that the slow overturning time of the global ocean (centuries to millennia) determines the responsiveness of MOT to changing climate, there is much interest in reconstructing ocean temperatures before the first observations (about AD 1872).

Marine proxies have produced such reconstructions on a variety of temporal and spatial scales[4–7]; however, the different proxies have strengths and weaknesses, leading to debate about the interpretation of the corresponding data (ref. 4 and references therein). The difficulty lies in separating temperature from other effects as well as assessing a precise proxy-to-temperature transfer function because of the complex biogeochemistry behind these proxies and potential regional as well as temporal differences[5,8]. Although trends in these proxies might be representative of the temperature trends, these issues are in particular problematic for the absolute accuracy of the corresponding temperature scale. The uncertainty of the absolute scale lies in the range[4,8] of ± 1 °C, which poses a major limitation for the determination of the glacial–interglacial MOT change (about 3 °C)[4].

Here we use a proxy for MOT introduced in ref. 9 based on measurements of inert or noble gas mixing ratios (Kr/N_2, Xe/N_2, Xe/Kr) in ice core samples (see Methods and ref. 10 for analytical details). The data are used to reconstruct past MOT with unequalled accuracy, taking advantage of the following characteristics of the ocean–atmosphere system: (1) any heat and gas exchange takes place at the ocean–atmosphere interface; (2) there are no essential internal heat sources or sinks in the ocean[11]; (3) there are no essential sources or sinks of the measured gases in the combined ocean–atmosphere system; and (4) each gas species has a unique and well defined temperature-dependent solubility. Therefore, a change in MOT leads to a change of the dissolved noble gas inventory in the ocean, which is in turn mirrored by an opposing change in the atmosphere without any intrinsic temporal delay or filtering (see detailed discussion in Methods). Because the atmosphere is well mixed this method effectively integrates globally. Thus, as opposed to marine proxies, the atmospheric noble gas ratio is a purely physics-driven proxy for the global ocean heat content and MOT[9,11].

We analysed 78 ice samples (including ten partial to full sample rejections; see Methods) from the WAIS Divide ice core that cover the Last Glacial Maximum (LGM) to the pre-industrial period. For the period 22–8 kyr BP (thousands of years before 'present', that is, AD 1950)—which contains the last glacial transition (20–10 kyr BP)—a high temporal resolution of 250 yr on average was obtained. Together with the rich information available from the same ice core and the excellent age control in this climate archive, our record allows unprecedented insights into the interplay between climate and MOT during a period of major climate change.

Inferring MOT from noble gases

To derive the atmospheric ratios needed for the MOT reconstruction, the raw data has to be corrected for gravitational enrichment and thermal fractionation in the firn column[12]. As in refs 9 and 10, we use the measured argon isotope ratio $\delta^{40}Ar$ ($^{40}Ar/^{36}Ar$) to correct the elemental ratios for the gravitational fractionation. The correction we apply assumes that the firn air column is in full thermal–gravitational equilibrium, which might not have been the case, as indicated by the difference between the $\delta^{86}Kr$ ($^{86}Kr/^{82}Kr$) and $\delta^{40}Ar$ (see Methods). This anomaly in $\delta^{86}Kr$ is a phenomenon that needs to be investigated further; however, it is roughly constant over the entire record, suggesting that the potential bias is small on relative changes within the record (but might have an effect on the absolute scale of about 0.3 °C—see below and Methods for more details).

[1]Scripps Institution of Oceanography, University of California San Diego, La Jolla, California 92037, USA. [2]Climate and Environmental Physics, Physics Institute, and Oeschger Center for Climate Research, University of Bern, 3012 Bern, Switzerland. [3]Laboratory for Air Pollution/Environmental Technology, Empa, 8600 Dübendorf, Switzerland. [4]National Institute of Polar Research, Research Organizations of Information and Systems, 10-3 Midori-cho, Tachikawa, Tokyo 190-8518, Japan. [5]Department of Polar Science, Graduate University for Advanced Studies (SOKENDAI), 10-3 Midori-cho, Tachikawa, Tokyo 190-8518, Japan. [6]Institute of Biogeosciences, Japan Agency for Marine-Earth Science and Technology, 2-15 Natsushima-cho, Yokosuka 237-0061, Japan.

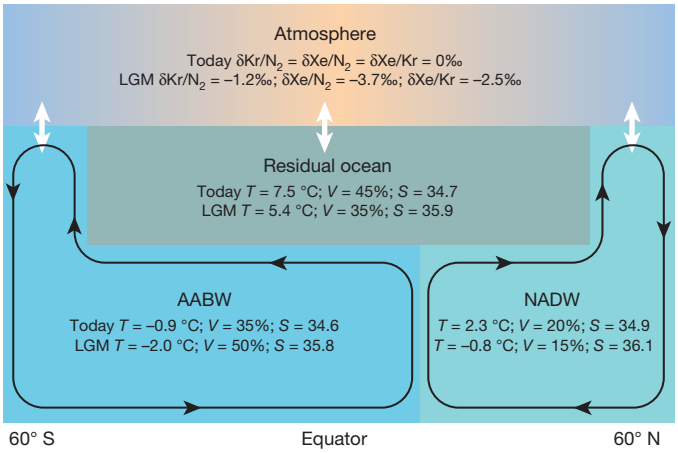

Figure 1 | Schematic of the four-box model used to derive MOT, including the modern ('Today') and LGM characteristics of the boxes. The shape and location of the boxes indicates roughly their zonally averaged situation in the modern ocean. Black arrows indicate the meridional circulation pattern of the two deep-water masses AABW and NADW. White arrows indicate the exchange of noble gases between the boxes and the geographical area in which they occur. The modern temperatures T, volumes V (as fraction of the total ocean) and salinities S (in units of the practical salinity scale, PSS) of AABW and NADW are based on ref. 20, while the parameters for the residual ocean are chosen such that the budget for the global average ocean ($T = 3.53$ °C; $S = 34.72$ PSS; $V = 100\%/1.34 \times 10^{18}$ m^3) is closed. The LGM parameters are based on the scaling of volume and salinity as well as the constraints from the noble gas data (see Methods for more details).

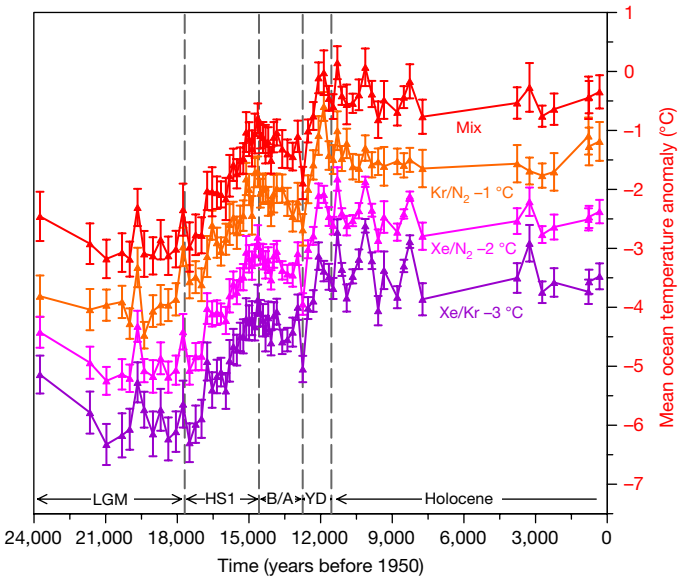

Figure 2 | MOT records relative to today derived from three different atmospheric noble gas ratios and their mixture. The records are based on 69 individual ice core samples with a distinct age (WD2014 age scale[36]), and each sample provides a separate value for atmospheric Kr/N_2, Xe/N_2 and Xe/Kr (if not subject to rejections; see Methods). Dashed vertical lines and labels mark different time periods (B/A, Bølling–Allerød; YD, Younger Dryas), as also in Fig. 3. The 'Mix' MOT record (red; best estimate) is not shifted, whereas the records based on the individual ratios are shifted as follows for better visibility: Kr/N_2 (orange) by −1 °C, Xe/N_2 (magenta) by −2 °C, Xe/Kr (purple) by −3 °C. Deviations of the individual records relative to each other are in Methods. The mean values and their error bars (1σ) include all analytical uncertainties and different scenarios as described in Methods.

The thermal fractionation correction is minor at the WAIS Divide ice core site owing to high accumulation rates and the gradual surface temperature changes[13], which limit the temperature differences over the length of the firn column to about 1 °C. The effects are, however, not negligible (approximately 0.25 °C change in MOT per 1 °C difference). Therefore, we correct our data for the thermal fractionation using two independent firn column temperature scenarios which represent the range of uncertainty of this correction element (see Methods). For our analysis below we combine the two scenarios in a Monte Carlo fashion to incorporate this uncertainty into our final best-estimate record.

To reconstruct MOT from the palaeo-atmospheric Kr/N_2, Xe/N_2 and Xe/Kr ratios, we use a four-box ocean–atmosphere model based on refs 9 and 10 (Fig. 1 and Methods). To account for changes in sea-level pressure, ocean volume and salinity, which affect the inventory of soluble gases in the ocean, we use the sea-level record of ref. 14. For each gas ratio 12,000 Monte Carlo MOT realizations are calculated that incorporate analytical uncertainties, uncertainties of the sea-level record, the degree of gas saturation, and those related to the applied firn thermal correction mentioned above (more details in Methods). We combine all realizations (36,000 in total) to a single best-estimate record (Fig. 2, red, 'Mix'). In this way, the obtained uncertainty accounts for inconsistencies between the estimated and effective thermal fractionation factors, for biases of the single-ratio MOT records (see Methods), as well as for all known model and analytical uncertainties. Thus, our uncertainty estimate is representative of the relative changes within our MOT record. Note that the uncertainty does not account for the potential bias induced by firn air disequilibrium mentioned above. Figure 3b shows a splined version of our best-estimate record with a low cut-off frequency so as not to dampen sharp features in our record; however, caution is required when interpreting excursions based on single data points, such as (for example) around 20 kyr BP.

Glacial–interglacial MOT difference

On the basis of our best-estimate record we determine the MOT change from the LGM to the Early Holocene (averaging periods marked by grey bars in Fig. 3) to 2.57 ± 0.24 °C (1σ). This is comparable to the estimates from marine proxies[4] of 3 ± 1 °C. The major contribution to the uncertainty estimate originates from a possible change in saturation state of the gases in the ocean. Today, the deep-water masses are slightly undersaturated with noble gases with respect to the water temperature[15,16]. During the LGM this undersaturation could have been reduced by about 50%, which would cause a bias in the LGM MOT of 0.24 °C in our best-estimate record (see Methods for more details). All other sources of uncertainty are of minor or negligible importance for this part of the analysis.

Even though MOT changes are related indirectly to average sea surface temperature (ASST) changes, which are in turn related to global average surface temperatures (GAST)—both important numbers for estimates of Earth system sensitivity[8,17–19]—it is not straightforward to constrain the LGM–Holocene ASST or GAST change from the MOT change we derive here. The main deep-water masses such as Antarctic Bottom Water (AABW) and North Atlantic Deep Water (NADW)—which represent today about 55% of the global ocean volume—are ventilated and thermally equilibrated in high-latitude areas[20,21] around 60°. Therefore, MOT is biased towards the polar regions in its representation of ASST. Furthermore, multiple lines of evidence suggest that the glacial deep water circulation was fundamentally different from today's, with a more stratified ocean and a larger AABW cell at the expense of the other water masses[22–25]. On the one hand, if one considers that surface temperature changes are amplified in higher latitudes compared to lower latitudes—a well known climate phenomenon known as polar amplification—one could argue that our LGM–Holocene MOT change represents an upper limit of average SST change. On the other hand, it is not clear by how much the changes in ocean circulation have affected the relevant areas for global ocean ventilation[21].

To explore these different aspects that link ASST and GAST to MOT, we evaluated oceanic and atmospheric temperature fields of

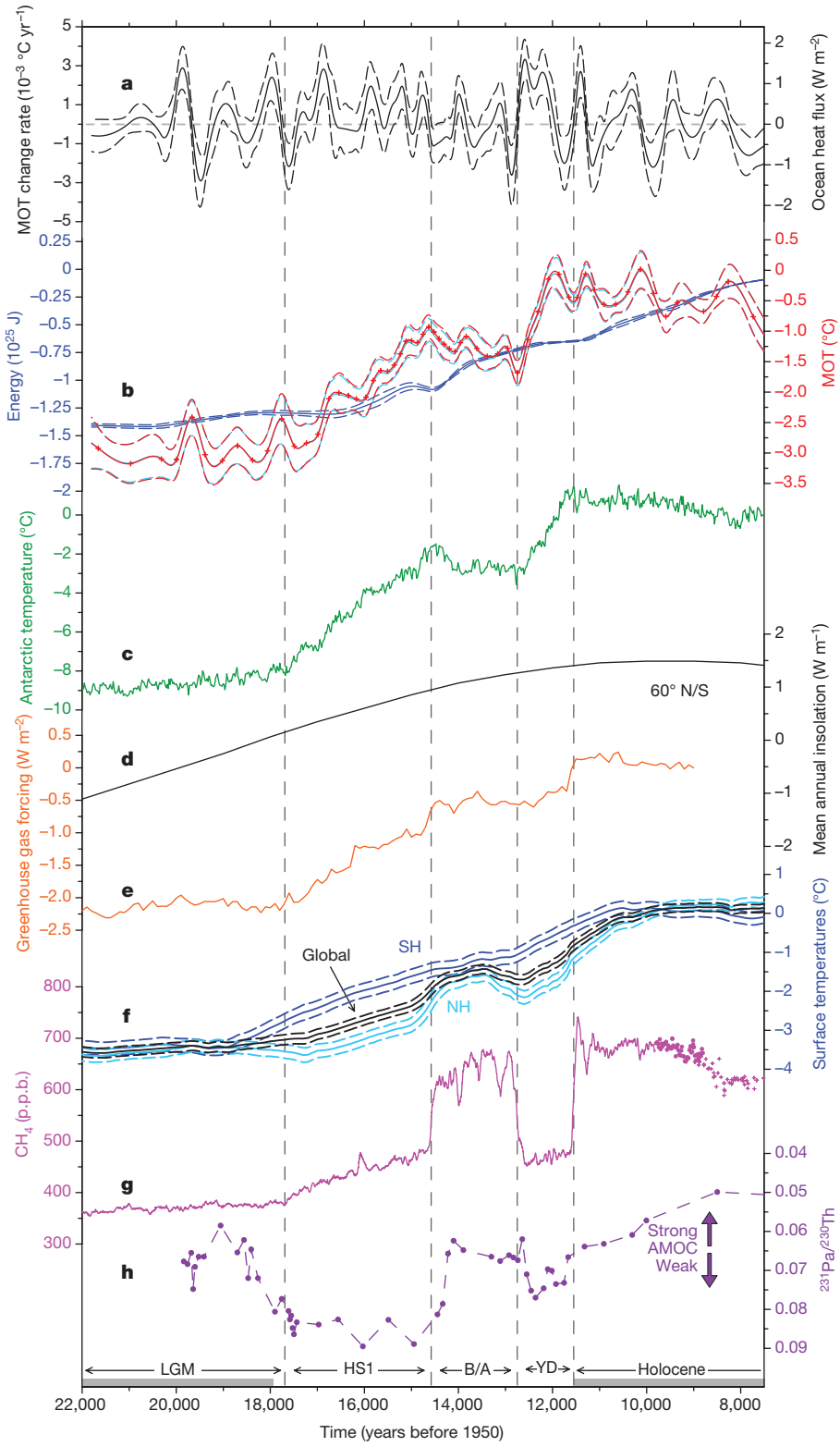

Figure 3 | Comparison of our best-estimate MOT record with other palaeoclimatic records for the last glacial transition. Labels as in Fig. 2. The grey bars mark the sections used to derive the LGM–Holocene MOT difference. **a**, MOT change rate and corresponding global ocean heat flux derived from Monte Carlo splining of our best-estimate MOT dataset with 600-yr cut-off frequency splines. The uncertainty band (dashed lines) represents the 1σ range of all realized Monte Carlo splines. **b**, The red lines are the splined version of our best-estimate MOT dataset (Fig. 2, red) using the same splining procedure as in **a**. Note that caution is required when interpreting excursions based on single data points, such as for example, around 20 kyr BP (also applies to **a**). The light-blue lines are the energy anomaly in the total ocean relative to today expressed in the same type of spline as for the red curve. The left *y* axis is scaled such that the light-blue and red curves overlap as much as possible. The remaining small difference originates from the different effect of ocean volume change on the two parameters. Crosses indicate where the actual data points are located. The dark-blue lines are the sea-level anomaly record of ref. 14 transferred into the latent energy put into melting (grounded) ice to create the corresponding sea-level change (the LGM low corresponds to a sea level 134 m below today's). The splining procedure is the same as above, but with a cut-off frequency of 150 yr (because of the higher resolution of this record) and a 2σ uncertainty band. The latent heat is derived by simple scaling of the sea-level data by 3.45×10^{14} m^3 ocean volume change per metre of sea level[14] and the latent heat coefficient for the ice–water transition (thermal expansion contribution (about 0.6 m between the LGM and the Holocene) can be neglected). **c**, Antarctic temperature reconstruction[39]. **d**, 60° N and 60° S (roughly where deep waters are formed) mean annual insolation anomaly relative to today[40], which is driven by changes in obliquity and is symmetric on both hemispheres. **e**, Greenhouse gas forcing[41]. **f**, Reconstructed Earth surface temperatures with 1σ uncertainty band of Northern Hemisphere ('NH', light blue), Southern Hemisphere ('SH', dark blue), and global average ('Global', black)[6]. **g**, Atmospheric CH_4 measured at the WAIS divide ice core[29]. **h**, AMOC proxy ^{231}Pa/^{230}Th from ocean sediment core OCE326-GGC5 recalibrated with IntCal13[30,42]. All data are plotted on their original age scale if not otherwise noted (WD2014 for WAIS data[36]). Note that the data shown in **b**–**f** are anomalies relative to today.

seven different global climate models (six are part of the Paleoclimate Modelling Intercomparison Project 3 (PMIP3)) that provided such output for LGM and preindustrial conditions (see Methods). All these independent state-of-the-art climate models have different but physically consistent climatologies for the two climate states, for which reason the model ensemble spread is representative of the uncertainties of how MOT, ASST and GAST are linked. The model ensemble ranges of the scaling factor for ΔASST/ΔMOT and ΔGAST/ΔMOT are 0.7–0.9 and 2.0–2.9, respectively. The models generally underestimate the LGM–Holocene MOT difference (range 0.9 °C to 2 °C) relative to our results. Despite the uncertainties related to these scaling factors, they suggest that the LGM–Holocene GAST difference is between 5.1 °C and 7.5 °C, which is roughly consistent with the estimates of refs 8 and 19, but not with the low values of ref. 6 and in particular of ref. 26. Note that most of these studies use PMIP climatologies to infer GAST as we do here, however, they use surface temperature proxies that are recording local climate and are affected by ocean biogeochemistry. Owing to the globally integrative and purely physics-driven nature of the MOT proxy

we present here it might be possible to better constrain such estimates in the future and narrow down some of the uncertainties related to the LGM GAST.

It is interesting to note that since the LGM about the same amount of energy has gone into MOT as into melting grounded ice (Fig. 3b). This is not contradicting the understanding that most of the current anthropogenic warming has been taken up by the ocean even though only about 10 cm of sea-level rise (about half of the total rise of 19 cm since 1900) is attributed to melting of grounded ice[2], whose latent heat equivalent is only about 3% of the total energy taken up by the ocean[1]. The response of melting land ice to global warming is very much dependent on the geometry/configuration/sensitivity of the global ice sheets at a specific point in time[27]. Therefore, the 1:1 ratio of energy going into the ocean and melting grounded ice has to be regarded as an average over the whole last glacial transition and cannot be expected to hold for the anthropogenic warming. However, as a recent study has shown[28], including ice melting is important to close also the current global energy budget and can provide new insights into the mechanism behind recent decadal global temperature variabilities.

Climate–MOT interplay

There is no temporal uncertainty between the MOT and CH_4 records (Fig. 3g) because they were obtained from trapped air in the same ice core. Atmospheric CH_4 reacts quickly to changes in the northern and tropical regions (within decades) and has been measured with very high resolution and precision[29]. Therefore, it is an excellent time marker for the abrupt changes in Northern Hemisphere climate (dashed lines in Figs 2 and 3) related to variations in the Atlantic Meridional Overturning Circulation (AMOC), that separate the climate periods Heinrich Stadial 1 (HS1), the Antarctic Cold Reversal and the Younger Dryas from each other[30]. This allows a precise comparison between MOT and the changing climate and ocean circulations that are associated with the climate periods mentioned above (Fig. 3).

First, the comparison of the inflection points of MOT and abrupt changes in the CH_4 record shows no lead or lag of MOT relative to these events (with the exception of the end of the Younger Dryas; see below). In particular for the transition from the HS1 to the Antarctic Cold Reversal, the temporal constraints are strong owing to the high resolution of both the MOT and the CH_4 records. For this event we estimate the MOT inflection point to occur at $14{,}780 \pm 390$ yr BP. This is indistinguishable from the occurrence of the corresponding CH_4 change at $14{,}580 \pm 80$ yr BP. This constrains any possible phase shift between CH_4/AMOC change and MOT to be within a couple of centuries, at least for this point in time.

Second, the trends in the MOT record we present here are strikingly similar to those of Antarctic temperature (AAT) during the last glacial transition (Fig. 3). AAT and MOT show the same general evolution of stable temperatures during the LGM, followed by a moderate warming during HS1 (17,690–14,580 yr BP), a cooling during the Antarctic Cold Reversal (14,580–12,750 yr BP), a strong warming during the Younger Dryas (12,750–11,550 yr BP) before reaching stable Holocene values. In fact, the Younger Dryas MOT warming finished about 500 yr before the rapid CH_4 rise at 11,550 yr BP that marks the end of the Younger Dryas. The end of the Younger Dryas is an anomaly to the otherwise close relationship of MOT and AAT during the last glacial transition.

During the HS1 period, MOT changes at a rate of 0.67 ± 0.11 mK yr^{-1}, which corresponds to an energy uptake by the ocean of $(3.6 \pm 0.52) \times 10^{21}$ J yr^{-1} (all errors given in this paragraph are 1σ). This is about 30% of what is estimated[1] for the ocean heat uptake between 1997 and 2015 ($(12.4 \pm 5.0) \times 10^{21}$ J yr^{-1}). The Antarctic Cold Reversal period is characterized by a statistically significant cooling of the global ocean of -0.29 ± 0.13 mK yr^{-1}, which translates into an energy loss of $(-1.4 \pm 0.66) \times 10^{21}$ J yr^{-1}. The warming from 12,750 yr BP to 12,050 yr BP (referred to as YD1) within the Younger Dryas represents the strongest global ocean warming phase within our record. The MOT change rate is 2.5 ± 0.53 mK yr^{-1} and the corresponding energy uptake $(13.8 \pm 2.9) \times 10^{21}$ J yr^{-1}. This unprecedented natural MOT warming rate is comparable to the strong warming since 1997 estimated in ref. 1, but clearly surpasses the estimate therein for the multidecadal trend from 1971 to 2005 (see below). The close relation between our MOT record and AAT/AMOC changes as well as the strong warming during the YD1 are two intriguing features of our record and are discussed here in more detail.

The synchronicity of MOT and AAT during the last glacial transition is somewhat surprising because AAT (and atmospheric CO_2) seems to lead global averaged surface temperatures (GAST) by several centuries[6] (Fig. 3f). However, this is not a contradiction because the lag of GAST relative to AAT/CO_2 is explained by a lag of the Northern Hemisphere temperatures (N-GAST) while the Southern Hemisphere temperatures (S-GAST) are synchronous with (or even lead) AAT/CO_2. MOT is a S-GAST-biased parameter owing to the larger volume of the ocean ventilated in the Southern Hemisphere[20,22], so the synchronicity of MOT and AAT/CO_2 is consistent with GAST lagging AAT/CO_2, as found in ref. 6. The general picture arising from this is that MOT, CO_2 and S-GAST are changing synchronously (within the given uncertainties) and N-GAST is lagging during the last glacial transition. With the glacial atmospheric CO_2 rise attributed to the release of CO_2 from the Southern Ocean[31], this suggests that (at least for this transition) the Southern Hemisphere climate was driving the global climate out of the glacial period and not the Northern Hemisphere. The similarity between AAT/AMOC and MOT could be explained such that only the waters ventilated at the high southern latitudes have a net effect on MOT. Through the well known AMOC-related meridional surface heat transport mechanism known as the bipolar seesaw[32], the Southern Ocean surface temperatures increase when the AMOC is in a weak state and vice versa. These surface temperature changes may have reached the southern deep-water formation areas and subsequently changed the temperatures of the AABW, which comprises a large portion of the global ocean volume. Changes in other regions might not necessarily have a net effect on MOT. This simple explanation suggests that the current ocean heat uptake could indeed be underestimated or undersampled given that AABW forms in the Southern Ocean and fills the bottom part of the ocean below 2,000 m, areas which are inadequately covered by observation systems such as the Argo floats[3].

However, this purely Southern-Ocean-driven explanation for the AMOC–MOT relation might be too simplistic. The basic behaviour of MOT increase during a weak AMOC and vice versa is seen in two model experiments[11,33], but it is explained by changes in the low-latitudinal ocean. The change in AMOC affects the heat capacity of the low-latitudinal Atlantic, which leads to accumulation of heat in this region after a switch from a strong to weak AMOC (such as from LGM to HS1) and a release of heat in the opposite case (such as from HS1 to the Bølling–Allerød period)[33]. This mechanism produces very similar MOT patterns and rates of change in the experiments of ref. 33 to what we find for the HS1 and Bølling–Allerød periods, providing some support for this underlying mechanism. However, this mechanism is not sufficient to explain the MOT pattern and rates of change during the Younger Dryas, where we find a much stronger warming in the first phase (about 700 yr), followed by temperature stabilization. In fact, this pattern is more comparable to what ref. 11 simulate in their AMOC disturbance experiments, though the magnitude of change in these experiments is quite different. In summary, the relationship between AMOC strength and MOT is a consistent feature in the few model studies that investigate the tie between these parameters, but neither study replicates the temporal pattern or magnitude of MOT change observed in this record.

So far we have looked into the ways that changes in AMOC could affect MOT. The causality, however, may be flipped: MOT may affect the AMOC. As shown in ref. 34, changes in Southern Ocean surface heat flux can affect the stability of the AMOC. If southern heat fluxes are high, the AMOC is stronger, and vice versa, because a warmer/colder Southern Ocean is associated with a warmer/colder AABW,

which reduces/increases the density differences between NADW and AABW and, hence, increases the pull/push onto the AMOC. In fact, the two causal relations mentioned here (effect of the AMOC onto MOT and vice versa) could provide a feedback loop that explains the fluctuations of the AMOC characteristic of the glacial periods[23]: during a weak AMOC state, the Southern Ocean/AABW warms[33], which decreases the density differences between NADW and AABW, continuously increasing the 'pull' onto the AMOC. Once the 'pull' becomes too large, the AMOC switches to its strong state, which in turn starts cooling AABW, making it again harder for the AMOC to sustain its strength as AABW becomes denser again. In other words, the bipolar seesaw and the teleconnection between Southern Ocean and AMOC together would make up a density oscillator which could—depending on the background ocean temperatures or stratification[34]—be self-sustaining and not necessarily triggered by a North Atlantic surface perturbation, often thought to be the cause behind the glacial AMOC fluctuations. This density oscillator is probably not only temperature-driven but also involves salinity changes. As outlined in ref. 22, Southern Ocean temperatures also affect the sea ice extent and the associated effect of brine rejection on the salinity/density of the Southern Ocean waters potentially exceeds the temperature effect on AABW density by up to a factor of five. The idea described here needs thorough testing with ocean models, and does not explain, for example, the abruptness of the AMOC changes that are characteristic to these AMOC changes in glacial times. However, it provides an alternative to the otherwise North-Atlantic-focused explanations for these oscillations and is in line with the MOT record presented here.

Younger Dryas warming

The strong YD1 MOT warming is a striking element of our record and represents a clear anomaly to the otherwise strong link between MOT, AAT and AMOC, respectively. The event starts at the same time as the corresponding warming events seen in the AAT and GAST records, but MOT shows a clearly higher warming rate and reaches its Holocene level considerably earlier. The correction of our data for the firn fractionation processes is critical, but neither do the stable isotope data used to derive this correction show any inconstancy nor does the uncertainty in the thermal correction have enough leverage to explain this event (see Methods).

There is an unexpected change in the accumulation rate in the WAIS Divide ice core from 12,000 yr BP to 11,600 yr BP[35], which could cause weakly understood dynamic firn fractionation processes, but this event had no effect on the YD1 part of the noble gas record because the air was already trapped in the ice before the accumulation event started (the uncertainty[36] in gas age versus ice age is only $\pm$50 yr). Therefore, the YD1 noble gas changes found here seem to be truly atmospheric. We cannot exclude the possibility that the ocean circulation pattern has shifted rapidly from its potential glacial state[22] to its modern state during the YD1, which could cause a dampening of the YD1 MOT change by up to 0.35 °C (the sum of the Kr and Xe saturation state and the AABW volume biases; see Methods) because we currently assume a gradual change. There is no evidence that such a change happened specifically at this point in time, for which reason we continue with the gradual change assumption. Nevertheless, this 22% leverage with which to dampen the YD1 MOT event still leaves the YD1 as an extreme event in terms of MOT warming.

The YD1 phase is associated with a strong ocean heat uptake of 1.1 ± 0.23 W m^{-2} (1σ), but the greenhouse gas forcing is basically stable, the orbital forcing change is negligible, the sea-level record does not indicate any major losses of land ice or albedo[14] (Fig. 3b), and other processes tend rather to a slight negative radiative forcing[37]. This suggests that the YD1 MOT warming is driven by ocean dynamics rather than by radiative forcing changes. The drainage of Lake Agassiz probably drove the AMOC changes during the Younger Dryas[37]; however, AMOC-disturbance experiments using intermediate complexity climate models either do not reproduce the high MOT warming rate of YD1 (1.6 °C in about 700 yr)[33], or fail to sustain this high rate over the observed period[11]. This suggests that AMOC changes can explain only part of the YD1 MOT warming. In experiments using state-of-the-art global climate models forced by anthropogenic greenhouse gas emissions[1], none of the 15 models (individually averaged over all realizations) reaches the warming rate of YD1 averaged over 1971–2005 (35 yr). The mean rate over all models is about a third of the YD1 warming rate, even though the greenhouse-gas radiative forcing is at least ten times stronger than during YD1[38]. In summary, this shows that the YD1 MOT warming is challenging the current understanding of global ocean temperature regulation and suggests that either current climate models generally underestimate the ability of the ocean to take up heat, or that climate conditions/drivers during the YD1 have been substantially different from the model experiments mentioned here in a way that allows much stronger heat uptake. Two ideas about possible conditions/drivers behind the YD1 warming are further discussed in Methods and are related to the strong insulation in high latitudes during YD1 (see Fig. 3d) and an isolated water mass combined with a drastic change in the global ocean overturning circulation, respectively.

In summary, the MOT reconstruction for the last glacial transition we present here constrains MOT with unprecedented accuracy from a novel proxy based on noble gases in the atmosphere. The record provides unique insights into the energy budget of the currently largest energy buffer in the climate system—the ocean—and its interplay with changing climate and ocean circulation. The insights we gain here raise questions about how the ocean regulates its temperature under variable conditions—a topic very important for future climate change—but have not yet been studied extensively owing to a lack of long-term reconstructions. We describe here the general features of the data and possible explanations for them, but further work is needed using global climate models to test our hypotheses.

Online Content Methods, along with any additional Extended Data display items and Source Data, are available in the online version of the paper; references unique to these sections appear only in the online paper.

Received 31 March; accepted 17 November 2017.

1. Gleckler, P. J., Durack, P. J., Stouffer, R. J., Johnson, G. C. & Forest, C. E. Industrial-era global ocean heat uptake doubles in recent decades. *Nat. Clim. Chang.* **6,** 394–398 (2016).
2. Stocker, T. F. *et al.* (eds) *Climate Change 2013: The Physical Science Basis. Contribution of Working Group I to the Fifth Assessment Report of the Intergovernmental Panel on Climate Change* (IPCC, 2013).
3. Abraham, J. P. *et al.* A review of global ocean temperature observations: implications for ocean heat content estimates and climate change. *Rev. Geophys.* **51,** 450–483 (2013).
4. Elderfield, H. *et al.* Evolution of ocean temperature and ice volume through the mid-Pleistocene climate transition. *Science* **337,** 704–709 (2012).
5. Elderfield, H. *et al.* A record of bottom water temperature and seawater δ^{18}O for the Southern Ocean over the past 440 kyr based on Mg/Ca of benthic foraminiferal *Uvigerina* spp. *Quat. Sci. Rev.* **29,** 160–169 (2010).
6. Shakun, J. D. *et al.* Global warming preceded by increasing carbon dioxide concentrations during the last deglaciation. *Nature* **484,** 49–54 (2012).
7. Shakun, J. D., Lea, D. W., Lisiecki, L. E. & Raymo, M. E. An 800-kyr record of global surface ocean δ^{18}O and implications for ice volume-temperature coupling. *Earth Planet. Sci. Lett.* **426,** 58–68 (2015).
8. Snyder, C. W. Evolution of global temperature over the past two million years. *Nature* (2016).
9. Headly, M. A. & Severinghaus, J. P. A method to measure Kr/N_2 ratios in air bubbles trapped in ice cores and its application in reconstructing past mean ocean temperature. *J. Geophys. Res.* **112,** D19105 (2007).
10. Bereiter, B., Severinghaus, J. & Kawamura, K. New method for measuring atmospheric heavy noble gas isotope and elemental ratios in ice core samples. *Rapid Commun. Mass Spectrom.* (in the press).
11. Ritz, S. P., Stocker, T. F. & Severinghaus, J. P. Noble gases as proxies of mean ocean temperature: sensitivity studies using a climate model of reduced complexity. *Quat. Sci. Rev.* **30,** 3728–3741 (2011).
12. Severinghaus, J. P., Sowers, T., Brook, E. J., Alley, R. B. & Bender, M. L. Timing of abrupt climate change at the end of the Younger Dryas interval from thermally fractionated gases in polar ice. *Nature* **391,** 141–146 (1998).
13. Cuffey, K. M. *et al.* Deglacial temperature history of West Antarctica. *Proc. Natl Acad. Sci. USA* **113,** 14249–14254 (2016).
14. Lambeck, K., Rouby, H., Purcella, A., Sunc, Y. & Sambridgea, M. Sea level and global ice volumes from the Last Glacial Maximum to the Holocene. *Proc. Natl Acad. Sci. USA* **111,** 15296–15303 (2014).

15. Hamme, R. C. & Severinghaus, J. P. Trace gas disequilibria during deep-water formation. *Deep. Sea Res. I* **54,** 940–950 (2007).
16. Loose, B. *et al.* Estimating the recharge properties of the deep ocean using noble gases and helium isotopes. *J. Geophys. Res. Oceans* **121,** 5959–5979 (2016).
17. Bindoff, N. L. *et al.* Detection and Attribution of Climate Change: from Global to Regional. In *Climate Change 2013: The Physical Science Basis. Contribution of Working Group I to the Fifth Assessment Report of the Intergovernmental Panel on Climate Change* (eds Stocker, T. F. *et al.*) Ch. 10, 867–952 (2013).
18. Knutti, R. & Hegerl, G. C. The equilibrium sensitivity of the Earth's temperature to radiation changes. *Nat. Geosci.* **1,** 735–743 (2008).
19. Annan, J. D. & Hargreaves, J. C. A new global reconstruction of temperature changes at the Last Glacial Maximum. *Clim. Past* **9,** 367–376 (2013).
20. Johnson, G. C. Quantifying Antarctic Bottom Water and North Atlantic Deep Water volumes. *J. Geophys. Res.* **113,** C05027 (2008).
21. Gebbie, G. & Huybers, P. How is the ocean filled? *Geophys. Res. Lett.* **38,** L06604 (2011).
22. Ferrari, R. *et al.* Antarctic sea ice control on ocean circulation in present and glacial climates. *Proc. Natl Acad. Sci. USA* **111,** 8753–8758 (2014).
23. Piotrowski, A. M., Goldstein, S. L., Hemming, S. R., Fairbanks, R. G. & Zylberberg, D. R. Oscillating glacial northern and southern deep water formation from combined neodymium and carbon isotopes. *Earth Planet. Sci. Lett.* **272,** 394–405 (2008).
24. Sigman, D. M., Hain, M. P. & Haug, G. H. The polar ocean and glacial cycles in atmospheric CO_2 concentration. *Nature* **466,** 47–55 (2010).
25. Bereiter, B. *et al.* Mode change of millennial CO_2 variability during the last glacial cycle associated with a bipolar marine carbon seesaw. *Proc. Natl Acad. Sci. USA* **109,** 9755–9760 (2012).
26. Schmittner, A. *et al.* Climate sensitivity estimated from temperature reconstructions of the Last Glacial Maximum. *Science* **334,** 1385–1388 (2011).
27. Levermann, A. *et al.* The multimillennial sea-level commitment of global warming. *Proc. Natl Acad. Sci. USA* **110,** 13745–13750 (2013).
28. Berger, A., Yin, Q., Nifenecker, H. & Poitou, J. Earth's future slowdown of global surface air temperature increase and acceleration of ice melting. *Earth's Future* **5,** 811–822 (2017).
29. Rhodes, R. H. *et al.* Enhanced tropical methane production in response to iceberg discharge in the North Atlantic. *Science* **348,** 1016–1019 (2015).
30. McManus, J. F., Francois, R., Gherardi, J.-M., Keigwin, L. D. & Brown-Leger, S. Collapse and rapid resumption of Atlantic meridional circulation linked to deglacial climate changes. *Nature* **428,** 834–837 (2004).
31. Anderson, R. F. *et al.* Wind-driven upwelling in the southern ocean and the deglacial rise in atmospheric CO_2. *Science* **323,** 1443–1448 (2009).
32. Stocker, T. F. & Johnson, S. J. A minimum thermodynamic model for the bipolar seesaw. *Paleoceanography* **18,** 1087 (2003).
33. Galbraith, E. D., Merlis, T. M. & Palter, J. B. Destabilization of glacial climate by the radiative impact of Atlantic Meridional Overturning Circulation disruptions. *Geophys. Res. Lett.* **43,** 8214–8221 (2016).
34. Buizert, C. & Schmittner, A. Southern Ocean control of glacial AMOC stability and Dansgaard–Oeschger interstadial duration. *Paleoceanography* **30,** 1595–1612 (2015).
35. WAIS Divide Project Members. Onset of deglacial warming in West Antarctica driven by local orbital forcing. *Nature* **500,** 440–444 (2013).
36. Buizert, C. *et al.* The WAIS Divide deep ice core WD2014 chronology—part 1: methane synchronization (68–31 ka BP) and the gas age–ice age difference. *Clim. Past* **11,** 153–173 (2015).
37. Renssen, H. *et al.* Multiple causes of the Younger Dryas cold period. *Nat. Geosci.* **8,** 946–949 (2015).
38. Joos, F. & Spahni, R. Rates of change in natural and anthropogenic radiative forcing over the past 20,000 years. *Proc. Natl Acad. Sci. USA* **105,** 1425–1430 (2008).
39. Parrenin, F. *et al.* Synchronous change of atmospheric CO_2 and Antarctic temperature during the last deglacial warming. *Science* **339,** 1060–1063 (2013).
40. Huybers, P. Early Pleistocene glacial cycles and the integrated summer insolation forcing. *Science* **313,** 508–511 (2006).
41. Marcott, S. A. *et al.* Centennial-scale changes in the global carbon cycle during the last deglaciation. *Nature* **514,** 616–619 (2014).
42. Reimer, P. *et al.* IntCal13 and Marine13 radiocarbon age calibration curves 0–50,000 years cal BP. *Radiocarbon* **55,** 1869–1887 (2013).

Supplementary Information is available in the online version of the paper.

Acknowledgements This work was supported by the Swiss National Science Foundation (scholarship P2BEP2_152071), by the US National Science Foundation (grants 05-38630 and 09-44343 to J.S.) and by the JSPS KAKENHI (grants 21671001, 26241011, 15KK0027 and 17H06320 to K.K.). We thank C. Buizert for providing the WAIS divide past firn temperature modelling results and P. Pfister for providing the Bern3D model results. We are deeply indebted to many participants in the WAIS Divide project and especially thank K. Taylor, M. Twickler, the National Ice Core Laboratory, the Ice Drilling Design and Operations (IDDO) for ice drilling, the New York Air National Guard for airlift, and the Office of Polar Programs of the US National Science Foundation. R. Keeling first provided the idea for the noble-gas-based determination of mean ocean temperature.

Author Contributions B.B. and D.B. performed the experiments and analysed the ice samples, and S.S. provided assistance. B.B. analysed the data and J.S. reviewed it. B.B. performed the simulations and data evaluations. J.S. supervised the project. K.K. developed central parts of the method used. B.B. drafted and wrote the manuscript and J.S., D.B. and S.S. reviewed it.

Author Information Reprints and permissions information is available at www.nature.com/reprints. The authors declare no competing financial interests. Readers are welcome to comment on the online version of the paper. Publisher's note: Springer Nature remains neutral with regard to jurisdictional claims in published maps and institutional affiliations. Correspondence and requests for materials should be addressed to B.B. (bereiter@climate.unibe.ch).

Reviewer Information *Nature* thanks W. Aeschbach, R. Stanley and the other anonymous reviewer(s) for their contribution to the peer review of this work.

METHODS

Deriving noble gas elemental and isotope ratios from ice cores. The analytical method we used to analyse the trapped air in the ice samples is described in ref. 10. Briefly, about 800 g of ice are melted in an evacuated vacuum vessel and the released air is cryo-trapped in a dip tube cooled with liquid helium. In a second step, the air is split into two subsamples and from one of them all non-noble gases are removed via a Zr/Al getter. Then, each of these two subsamples is analysed separately on a specific dual-inlet isotope ratio mass spectrometer. The two machines provide high-precision deviations (usually expressed in δ-notation) from a standard, which is in our case the current atmospheric composition. Specifically, the two machines provide the following main isotope ratios (mass ratios): $\delta^{15}N$ ($^{29}N_2/^{28}N_2$), $\delta^{40}Ar$ ($^{40}Ar/^{36}Ar$) and $\delta^{86}Kr$ ($^{86}Kr/^{82}Kr$); as well as the following main elemental ratios: $\delta Ar/N_2$ ($^{40}Ar/^{28}N_2$), $\delta Kr/Ar$ ($^{84}Kr/^{40}Ar$) and $\delta Xe/Ar$ ($^{132}Xe/^{40}Ar$). The elemental ratios of $\delta Kr/N_2$ ($^{84}Kr/^{28}N_2$), $\delta Xe/N_2$ ($^{132}Xe/^{28}N_2$) and $\delta Xe/Kr$ ($^{132}Xe/^{84}Kr$), which are used for the MOT reconstruction, are derived by combining the machine elemental ratios accordingly. The isotope ratios are used to correct for gravitational and thermal fractionation in the firn column as described in Methods subsection 'Inferring atmospheric noble gas ratios from the raw data'.

The dataset presented here was obtained over the course of three measurement campaigns in 2014 and 2015. The first campaign applied method 1 described in ref. 10 during which 21 samples of the WAIS Divide ice core were analysed. The results of two of the samples were fully or partly rejected owing to measurement artefacts or artefacts occurring in the bubble-to-clathrate-transition zone (BCTZ) of ice cores (see Methods subsection 'Sample rejection and the data gap from 4,000–7,500 yr ago') below). The second and third campaigns applied method 2 of ref. 10, in which 42 and 15 samples, respectively, from the same core were analysed. Six samples of the second campaign were partly or fully rejected for the same types of reasons as mentioned above; two rejections were required in the third campaign samples.

Sample rejection and the data gap from 4,000–7,500 yr ago. 10 out of the 78 samples we measured for this study are subject to sample rejections. For 3 of them, however, the entire set of data did not have to be rejected (partial rejections). Partial rejections can occur when a measurement error occurs after the sample splitting[10], thus affecting only the corresponding dataset. Another possibility is that a minor error only affects the parameters that are most sensitive to it: for example, a thermal gradient during the splitting process will affect $\delta Ar/N_2$ the most because of its strong thermal diffusion sensitivity[43] relative to the precision obtained[10]. Depending on the amplitude of such an error, some parameters might appear as outliers, while others do not. It is therefore important to check all parameters thoroughly and individually and put them into the context (if possible) of the whole record, as done for the example of the BCTZ in ref. 10. For the first case (affecting one subsample), we have two such cases where the primary heavy noble gas data was lost owing to a failure of the corresponding mass spectrometer. For the second case of single parameter outliers, we rejected the data including Xe, but kept the remaining parameters. These affected samples could be replaced by measuring a neighbouring sample.

The full rejections affect 7 samples, of which one is related to operational errors during the measurement procedure and another one to a contaminant in the sample. These two samples could also be replaced by measuring a neighbouring sample. The remaining 5 of these full rejections are related to gas fractionation in the BCTZ, which creates a data gap[10] in our record from about 4,000–7,500 yr BP that can only be filled with measurements from another core. In the BCTZ, gases are fractionated due to gas-loss and fractionation processes between the bubbles and clathrates occurring in this zone[44,45]. We identified this zone primarily by inconsistencies or outliers in $\delta Ar/N_2$ with respect to $\delta^{40}Ar$ ($^{40}Ar/^{36}Ar$)as seen in ref. 44, but we also looked for inconsistencies in all other observed isotope and element ratios[10]. The BCTZ is also known as the brittle ice zone[46] because of the very brittle behaviour of the ice core and is often reported as such by the drilling team. However, the way we observe the BCTZ through the gas measurements does not necessarily line up with the observation via the core quality or the appearance/disappearance of clathrates and bubbles in the ice. The reason is that at the upper end of the BCTZ some fractionation has to build up in order to obtain noticeable effects from the gas diffusion processes in the extracted air, and at the lower end, the gas fractionation can 'tail' into the fully clathrated ice zone[45]. Hence, we expect the alterations in the gas record due to the BCTZ which we observe via the gas measurements to be shifted downwards in depth compared to the zone defined by the core quality and inclusion observations; however, it is not clear to what extent. It was a goal of this study and of ref. 10 to identify the BCTZ-affected zone for the parameters we obtained.

The top end of the BCTZ-affected zone was found between 922 m and 1,120 m depth and the bottom end was found between 1,510 m and 1,572 m depth[10], while the core quality and inclusion observations find the BCTZ or 'brittle ice zone' at 520–1,310 m depth[47,48]. This large shift of several hundred meters is surprising and has not been observed so far in other gas records; however, it is specific for the ice core and the gases we observe here and could also vary between different methods for the same gas species. Nevertheless, it is interesting to note that we find gas fractionation effects of the BCTZ to affect our data in a depth interval that is considerably deeper and slightly narrower than what the ice observations suggest.

A further quality control was done by comparing the reconstructed atmospheric $\delta^{18}O$ ($^{34}O_2/^{32}O_2$) values with the record of ref. 49. However, it turned out that this control is not very sensitive and did not uncover more outliers than those already identified with the parameters mentioned above. Nevertheless, it is important to check all these parameters to ensure the consistency of the great wealth of data the method provides, because many elements of this complicated method can alter the measurement[10]. The high quality of the record (outside the BCTZ) is probably attributable to careful core handling and processing under cold conditions (the ice-processing tent in the field was actively cooled to −25 °C)[50] and our subsamples were kept in a −50 °C freezer whenever possible to prevent outgassing[51].

Potential biases in MOT from noble gases in ice core samples. Concentration or ratio changes in the most prominent gases in the atmosphere (CO_2 and O_2) are the result of a combination of complex biogeochemical processes reacting or adapting to changing climate[49,52]. Therefore, these well studied gases contain an intrinsic delay and low-pass filtering behaviour with respect to climate change that are dependent on the inertia of the underlying mechanisms. In contrast, the noble gases analysed in this study are not subject to any biogeochemical process and their atmospheric changes are dependent only on their physical transportation in the atmosphere–ocean system. For our application here the relevant physical transportation processes are (1) the exchange between ocean and atmosphere, (2) the mixing within the atmosphere and (3) the transport from the atmosphere into the ice. We discuss these three elements in detail to show that they do not create a temporal modulation of the observed noble gases with respect to MOT.

All the heat fluxes in and out of the ocean take place at the ocean–atmosphere interface. There is no internal heat source in the ocean, and geothermal heating (the most potent heat source for the ocean besides the atmosphere/surface) is negligible compared to the forcing at the surface[11]. Hence, if the noble gas transport across the ocean–atmosphere interface is following the equilibrium solubility function as assumed here, for each joule going in or out of the ocean a corresponding number of noble gas molecules gets released from or dissolved in the ocean, respectively. Internal mixing of water masses with different temperatures mixes joules and noble gases in the same way. Although this would lead to local solubility disequilibrium in these mixed waters owing to the nonlinearity in the solubility functions, it does not affect the measured atmospheric composition, because this process takes place inside the ocean.

The assumption of gas equilibrium is justified because the gas transfer velocity between surface ocean and atmosphere of the observed gases lies in the range 13–16 cm h^{-1} (3 °C water temperature, 10 m s^{-1} wind speed)[53], which translates into an equilibration timescale for these gases of one to two months with a mixed layer of 200 m thickness as found in polar regions (shorter equilibration in other regions). This is short enough to capture the strong seasonality in the hemispheric ocean heat fluxes as evidenced by atmospheric measurements[54] of Ar/N_2, and is also much shorter than the residence time of water parcels in the mixed layer, in particular in the Southern Ocean, where gas equilibration is most critical[55]. There is a slight disequilibrium of noble gases in the deep ocean[15,16], but this does not affect the relatively fast equilibration timescales of the surface ocean. However, it has implications for the absolute scale of our proxy, as discussed below in Methods subsection 'Box model to infer MOT'. For these reasons, the ocean–atmosphere gas exchange does not create any delay or low-pass filtering behaviour of atmospheric noble gases with respect to climate change/ocean temperature changes in our record. This is also supported by the model simulation of ref. 11, which includes physical gas exchange processes and ocean circulations in a three-dimensional model. The ocean circulation perturbation experiments done in this study do not show any temporal modulation between the modelled ocean temperature and atmospheric noble gases.

Mixing within the atmosphere also takes place on timescales of months to a year, for which reason the studied gas mixing ratios probably contain geospatial differences on seasonal timescales[54] comparable to Ar/N_2. However, these seasonal variations are smoothed in the trapped air in ice core samples because of the low-pass filtering of the stagnant firn air column through which atmospheric signals have to be transported before they are trapped in the ice[56]. The filter time characteristic for the WAIS Divide ice core varies[29] between 20 yr and 50 yr, meaning that the trapped air in the ice is an average value over these time periods. This filter characteristic is in fact exceptionally low for Antarctic ice core standards and is a

result of the high accumulation rate at the site, for which reason the WAIS Divide ice core provides excellent temporal resolution capabilities for trapped gas in the ice. The firn filtering timescale is much lower than our maximum sampling rate of about 110 yr and is also substantially below the 600-yr cut-off frequency that we apply in the data splining. For all these reasons the noble gas records presented here contain no intrinsic temporal dampening element such as is known to occur in other atmospheric gas records and are (within the given uncertainties and the current understanding) a direct representation of MOT. There are, however, processes that can alter the scaling between noble gases and MOT; these are discussed and quantified in Methods subsections 'Inferring atmospheric noble gas ratios from the raw data' and 'Box model to infer MOT'.

There does exist a scenario under which our noble gas data would be blind to MOT changes: if there were a large portion of the ocean that exchanges heat with the atmosphere without exchanging gases. The corresponding water masses would be characterized by disequilibrium between temperature and dissolved noble gases, with the same magnitude of disequilibrium for all noble gases. Today, such waters seem not to exist because all deeper ocean water masses found so far contain an amount of noble gases corresponding to their temperature[15,16] (with a tendency to noble gas undersaturation, however, caused by fast cooling and not of the same magnitude for all noble gases; see also Methods subsection 'Inferring atmospheric noble gas ratios from the raw data'). The glacial ocean circulation pattern suggested in ref. 22 could have favoured the production of such 'blind' water masses during the LGM; however, it is important to note that our data would only be affected if these water masses were completely isolated from the atmosphere while exchanging heat before sinking into the deep ocean (conceivable if there were a gas-impermeable sea ice layer through which heat could be conducted, so that the waters underneath would sink into the deep ocean without any more atmospheric contact). If the sea ice were only partly or slowly permeable for noble gases or the waters had only a very short exposure time with the atmosphere (expected if polynyas (areas of open sea surrounded by ice) were as important for deep-water formation as they are today[57]), the 'blindness' would no longer exist. As soon as a slight exchange of gases occurred, Kr would come closer to equilibrium than Xe because of the faster equilibration time of Kr (similar concept as behind the fast-cooling effect[15]). Under such a situation our data would show a discrepancy between the MOT signal in $\delta Xe/N_2$ relative to $\delta Kr/N_2$ (because we assume constant equilibration over time; see also Methods subsection 'Inferring atmospheric noble gas ratios from the raw data') and, hence, be indicative of such a process (which is not the case). This scenario of 100% decoupling for a large portion of the ocean is conceivable under a Snowball Earth scenario, but seems very unrealistic and hypothetical for the LGM situation, because there is no indication that deep waters would form in such a way. However, further studies with state-of-the-art climate models are needed to rule out these unrealistic but not-yet-excludable effects. Note that if the LGM ocean had had such a 'blind' water mass, the transition from 'blind' to 'not blind' would have needed to happen immediately because an 'in between' state should appear as a phase of discrepancy between MOT values from $\delta Xe/N_2$ and $\delta Kr/N_2$ (which is not the case).

Inferring atmospheric noble gas ratios from the raw data. The heavy noble gas ratios we obtain from the ice core samples are highly fractionated with respect to the atmospheric value, mainly owing to gravitational fractionation in the static firn air column at the top of an ice sheet, below which the air is trapped in the ice. The depth of this firn column changes over time and is influenced by the local snow accumulation rate and temperature, among other things[58]. The effective firn air depth at a specific point in time can be 'measured' by analysing stable gas isotope ratios of N_2 ($\delta^{15}N$), Ar ($\delta^{40}Ar$), Kr ($\delta^{86}Kr$) and Xe ($\delta^{132}Xe$). By combining these ratios it is also possible to resolve the minor thermal and kinetic fractionation processes that might have occurred[59]. The conditions required for kinetic fractionation to occur—as described in ref. 59 (very low accumulation rate, low temperature)—do not apply to the WAIS Divide ice core drill site[13,36], for which reason this effect is not considered in our calculations and we consider only gravitational and thermal fractionation. With the method used in this study we obtain the atmospherically stable ratios of $\delta^{15}N$ ($^{29}N_2/^{28}N_2$), $\delta^{40}Ar$ and $\delta^{86}Kr$ ($^{86}Kr/^{86}Kr$) with a precision that enables us to resolve the thermal and gravitational fractionation processes adequately[10].

In theory—knowing all the air fractionation processes occurring in the firn column—the differences between the measured isotope ratios can be used to reconstruct the thermal fractionation component using the well known thermal diffusivity parameters[59,60]. Since we have three isotope ratio pairs but only one fractionation effect that should affect these values, the system is over-determined and we can check whether it is consistent for all possible combinations. However, any combination including $\delta^{86}Kr$ to determine the thermal component results in a temperature difference of 1.5 °C to 2 °C between the top and bottom of the firn column (referred to as the 'firn thermal gradient') for the LGM and Holocene periods, which is unrealistic because of the stable surface temperatures during these periods[13]. About the same constant offset is found during the transition period compared to the modelled firn thermal gradients of ref. 36. If $\delta^{15}N$ and $\delta^{40}Ar$ is used, the thermal component is in rough agreement with the expectations through the whole record. We have thoroughly tested our method for possible analytical artefacts that could fractionate or contaminate $\delta^{86}Kr$, without success. Also, if there were such an artefact, we would have corrected for it to a large extent given that we reference our ice sample measurements to modern air samples, which are measured on the concept of identical treatment[10].

To circumvent $\delta^{86}Kr$ in a first step, we use an independent scenario of firn thermal gradient based on ref. 36. After applying this scenario to the data we follow the approach of ref. 9 and use $\delta^{40}Ar$ to obtain the gravitational correction component for all other elements. $\delta^{40}Ar$ has the smallest analytical uncertainty per mass unit—1.5 per meg (that is, $1.5 \times 0.001‰$) on average—and hence, provides the highest possible accuracy for this largest, but well defined, correction factor. The isotope data that are corrected using this approach (Extended Data Fig. 1) show clearly that $\delta^{86}Kr$ is depleted relative to $\delta^{15}N$ and $\delta^{40}Ar$ (referred to as the 'Kr anomaly'), which is the reason why the firn thermal gradients based on $\delta^{86}Kr$ mentioned above turn out wrongly. We believe this Kr anomaly is a true signal in the trapped ice, probably caused by a firn fractionation mechanism that is yet unknown. Further investigations from other sites are needed for a better understanding of the mechanism behind it.

The Kr anomaly seems mainly to consist of a fairly constant offset relative to the other isotope of −56 per meg without any obvious trends and changes over time (Extended Data Fig. 1). This indicates that the underlying mechanism is fairly stable over time, for which reason we correct the $\delta^{86}Kr$ raw data by this average offset. If we use the corrected $\delta^{86}Kr$ values and compare the firn thermal gradients based on the different isotope pairs again, the results are now consistent with each other (the gradients involving $\delta^{86}Kr$ do now provide realistic and comparable values, as do the values based on $\delta^{15}N$ and $\delta^{40}Ar$ for the whole record period).

Therefore we derived a second scenario for firn thermal gradients based on the measured isotopes (including the corrected $\delta^{86}Kr$) by averaging the gradients derived from the three possible isotope pairs (see Extended Data Fig. 1b). This data-based scenario is independent of the first model-based scenario of ref. 36, and together the scenarios represent the uncertainty range associated with the thermal-correction component for our study. We account for this uncertainty range in our final MOT record by combining the 3,000 Monte Carlo MOT realizations of each scenario and propagate this uncertainty element into our final record (see more details in Methods subsection 'Box model to infer MOT'). In general, the uncertainty associated with this thermal correction is comparable to the one originating from the analytical uncertainties. The analytical uncertainties translate into about 0.2 °C uncertainty in MOT (see Methods subsection 'Potential biases in noble gases from ice samples as a proxy for MOT') whereas the effect of the two scenarios on our MOT estimate is within about 0.25 °C (corresponding to a 1 °C firn thermal gradient difference between the scenarios).

We cannot exclude the possibility that the underlying mechanism of the Kr anomaly also affects to some extent the gas ratios we use to reconstruct MOT ($\delta Kr/N_2$, $\delta Xe/N_2$, $\delta Xe/Kr$). As seen in Extended Data Fig. 2, the reconstructed atmospheric noble gas ratios are depleted during the Holocene period, which translates into an average Holocene MOT of −0.36 °C below present values, as seen in our MOT record in the main text (Fig. 2). This Holocene MOT 'offset' is more than the observed ocean warming since the industrialization[1] and, hence, would suggest that there was substantial MOT warming already before industrialization. This 'offset', however, could also be an artefact because the mechanism behind the Kr anomaly might also deplete $\delta Kr/N_2$, $\delta Xe/N_2$ and $\delta Xe/Kr$. Since the Kr anomaly seen in Extended Data Fig. 1 is fairly constant over time, the effect on $\delta Kr/N_2$, $\delta Xe/N_2$ and $\delta Xe/Kr$ is also expected to be constant over time, for which reason we argue that the mechanism behind the Kr anomaly produces—if any at all—a constant bias to our MOT record of perhaps −0.36 °C, but does not change the relative changes within our record. Therefore, relative changes, such as the Holocene–LGM MOT difference or the MOT trends of the different periods, are not affected by this potential bias and represent the effective changes in MOT. However, the readers have to be careful in interpreting the absolute values we derive from our records, because of the potential bias described here. Nevertheless, we do not apply any offset correction to our MOT record, as we do not feel confident to do so at present.

Despite the fact that the conditions at the WAIS Divide site do not fit the conditions required for kinetic fractionation as described in ref. 59, we tested this model and interpreted the Kr anomaly as caused by kinetic fractionation and used the model to scale the anomaly to the elemental ratios. With this approach, the resulting MOT records for the Late Holocene are found to be warmer than today by about 0.25 °C and not consistent with each other for the LGM period. Accordingly, the mechanism behind our gas fractionation must be somewhat different to kinetic fractionation.

One way to look at the Kr anomaly is that the heavier Kr—and therefore also slower diffusing gas in the firn air column—deviates from the lighter N_2 and Ar isotopes towards a smaller gravitational enrichment. This could be related to the relatively fast transformation of the WAIS Divide firn air column, which could lead to disequilibrium in the firn air such that the slow diffusing gases would not be able to 'catch up' with the fast downward advection of the ice matrix. This effect would be stronger the more slowly the gases diffuse through the air, which is (to first order) related to the weight of the molecule; hence N_2 and Ar would be less affected than the heavier gases like Kr and Xe. By using the isotopes of a light molecule to correct for gravity (δ^{40}Ar in our case) the gravitational component of the heavier molecules might be overestimated. This would be consistent with the depletion in the reconstructed atmospheric δ^{86}Kr (Extended Data Fig. 1a), and potentially also $\delta Kr/N_2$, $\delta Xe/N_2$ and $\delta Xe/Kr$. If this were the case, however, we would expect an even stronger 'anomaly' for Xe isotopes (δ^{132}Xe ($^{132}Xe/^{129}Xe$)) than for Kr isotopes (by about a factor of two, based on the diffusivity in air/total mass). For the data obtained in the last campaign (see Methods subsection 'Deriving noble gas elemental and isotope ratios from ice cores') we changed the mass spectrometer method so that we were able to obtain δ^{132}Xe (not shown here), though with much worse precision[10] than for δ^{86}Kr. The data indicates no anomaly for δ^{132}Xe, which is not what we expected, but the data are sparse and further work is needed to rule this out.

That a Kr anomaly (or $\delta^{86}Kr_{excess}$) is indicative for disequilibrium effects in the firn air column is shown by the firn air transport modelling study of ref. 61. The model, however, currently lacks experimental support, for which reason further firn air studies at different sites with different firn transformation characteristics are needed. For our purposes, such work would also need to include the effects on the heavy noble gases (isotopes and mixing ratios), in particular $\delta Kr/N_2$, $\delta Xe/N_2$ and $\delta Xe/Kr$. This has the potential to strongly reduce the current uncertainty of our MOT data, both on the absolute and relative scale.

Box model to infer MOT. To derive MOT from the heavy noble gas data, a box model is used as described in ref. 10. The basic assumption in the model is that N_2, Kr and Xe are conserved in the ocean–atmosphere system and that these gases are in solubility equilibrium between the two reservoirs. Hence, any change in ocean temperature changes the well defined equilibrium state of the noble gases. Since the solubilities of the individual gases are not equally sensitive to water temperature changes, the ocean temperature change leads to a change in atmospheric mixing ratio, which can be observed with ice cores. Here, the model is used backwards, using the measured atmospheric ratios as input and deriving the corresponding MOT by iteration. We use the same solubility functions as used in ref. 15 (which uses the solubility function of ref. 62 for N_2, of ref. 63 for Kr, and of ref. 64 for Xe) with the same 2% correction for the original Xe solubility function.

The first rough validation of this simple box model comes from the work of ref. 9, which showed an agreement of MOT derived from their noble gas ratios measurements in ice cores with the MOT independently derived from ocean sediment core proxies. Furthermore, the simple box model has been tested against a climate model with intermediate complexity[11] and also showed a negligible difference between the two models despite the large complexity difference. The same study also confirmed that the only non-surface heat source for the ocean—geothermal heating—is too small to affect the noble gas–MOT relation noticeably. However, in ref. 11 a sea ice gas-exchange effect is also implemented, which resulted in different noble-gas-to-MOT relationships from those of the non-sea-ice case. From the new noble gas data of this study, we can now conclude that their sea-ice effect is overestimated, as the corresponding $\delta Xe/N_2$ scaling would suggest an unrealistically low MOT for LGM of at least 4 °C below today (our −4‰ value for the LGM is no longer covered by their results).

Owing to the much higher quality of the noble gas data presented in this study, smaller effects not considered in ref. 9 can become relevant. Therefore, we implemented and tested different model elements to assess all possible sources of uncertainties within our box model. An overview of the different elements is shown in Extended Data Table 1, including the corresponding effects onto the LGM–Holocene MOT difference. The effects were derived by successively implementing the elements from top to bottom of the table.

The most minimalist model consists only of one ocean and one atmosphere box and uses only the measured noble gas ratios ($\delta Kr/N_2$, $\delta Xe/N_2$ or $\delta Xe/Kr$) to infer MOT. This model setting suggests the LGM MOT to be roughly −2.0 °C colder than the Holocene, which seems too low compared to the −2.5 °C to −3.5 °C suggested by sediment core proxies and model studies[4,5,7,11]. Nevertheless, we can assess the uncertainties of our MOT estimate within this minimalist model. The only source of uncertainty here is the analytical uncertainty which we propagate into the total MOT uncertainty using 3,000 Monte-Carlo simulations (3,000 realizations of MOT values while changing the noble gas ratios within their analytical uncertainties). The corresponding MOT uncertainty is on average ±0.26 °C for $\delta Kr/N_2$, ±0.15 °C for $\delta Xe/N_2$ and ±0.17 °C for $\delta Xe/Kr$, respectively, comparable to what is reported in ref. 10 for the individual methods.

As ref. 9 has already pointed out, sea-level change has an important effect on the noble gas distribution in the ocean–atmosphere system owing to the associated changes in ocean volume, ocean salinity and sea surface pressure. Salinity and sea surface pressure affects the solubility equilibrium state and the ocean volume defines the total storage capacity of the ocean. Here we use the sea-level change record from ref. 14 to derive these elements. Implementing the sea-level change effects increases the LGM–Holocene difference by 0.5 °C, with the largest contribution by the volume effect and the other two effects roughly compensating each other (see Extended Data Table 1). The uncertainty of the sea-level change record is also propagated into our total MOT uncertainty estimate; however, its contribution is below 10% of that of the analytical uncertainty.

The two elements included so far correspond to what has been implemented in the previous works already. We now investigate further elements that potentially have a considerable effect on our MOT reconstruction. The colder glacial climate is known to be drier than the interglacial/modern climate because of its lower water content. A lower water content also means a lower total mass of the atmosphere and hence, a lower average sea surface pressure. We estimate this effect using the current atmospheric H_2O concentration of about 2.5% (ref. 65) and a Clausius–Clapeyron relation of atmospheric H_2O concentration and temperature[66] while taking our MOT differences relative to today to be the effective surface temperature change. This approach might slightly underestimate the effective change in H_2O concentration/sea surface pressure because the average surface temperature change might have been slightly larger[6,67]; however, considering the small effect on the MOT reconstruction and the uncertainties related to such global surface temperature estimates, this approach is justified. For the sake of completeness, we implemented a linear change of this effect from the LGM to the beginning of the Holocene in our final MOT record.

The majority of the ocean volume gets its temperature and noble gas imprint, respectively, in the high latitudes around Antarctica where the largest portion of the deep water is formed[21]. In these regions the average sea surface pressure is slightly lower by about 3% compared to the average ocean surface[68]. We therefore assume a time-independent offset of the effective sea surface pressure by 3% to calculate the solubility equilibrium state in our box model. This slightly reduces the noble gas amounts dissolved in the ocean and causes the noble gas ratios to be less sensitive to MOT changes. Hence, this effect requires a slightly lower LGM temperature of −0.05 °C to compensate for the reduced sensitivity. Regional sea surface pressure changes between glacial and interglacial climate are simulated to be in the range of a few hectopascals[69], which is one to two orders of magnitude smaller than the global sea surface pressure effect from changing sea levels. Therefore we can assume this pressure bias to be time-independent.

As shown in refs 15 and 16, deep waters today are slightly undersaturated in Kr and Xe with respect to the water temperature. This phenomenon is explained by the strong cooling rate these waters experience before they sink into the deep ocean, preventing the noble gases from fully equilibrating with the waters before they sink[15]. The observed undersaturation is roughly 2% for Xe and 1.3% for Kr, respectively. Owing to the large differences expected in the glacial deep-water circulations compared to today[22], it is possible that this undersaturation pattern was different for glacial periods. As the general overturning of the deep circulation is expected to have been slower, it is likely that the cooling rate was smaller in glacial times and, hence, the undersaturation smaller. The most extreme case—where noble gases were in full equilibrium in glacial times—leads to unrealistically large discrepancies between the MOT derived from the different ratios. The change of undersaturation that keeps MOT differences roughly within the allowed uncertainty range is 50% (meaning that Xe undersaturation at LGM could have been 1% and Kr accordingly). This causes the LGM temperature derived from the different ratios to be up to 0.4 °C warmer as with a constant undersaturation (Xe/Kr being most sensitive followed by Xe/N_2, and almost no effect for Kr/N_2). Since the effective change in undersaturation is unknown, we calculate MOT realizations for the case with constant undersaturation at all times and a 50% change (linear) over the course of the LGM–Holocene transition (17,900–11,550 yr BP) and combine the two scenarios for our best-estimate record. This leads to a slight shift of the average MOT towards warmer temperatures and an increase in the uncertainty range for the earlier part of the record (see also LGM–Holocene MOT change estimate below).

AABW and NADW—which together represent more than half of the global ocean volume today and probably occupied even more in glacial times[22]—have different characteristics with regard to temperature and salinity (see also Fig. 1). Using only one ocean box in our model as done so far implies that the global temperature distribution in the ocean was the same as today and that all water masses changed their temperature equally. However, AABW is −0.88 °C today[20]

and its cooling potential is only about 1.2 °C before it reaches the freezing point of seawater (−2 °C), which is not enough to fulfil the constraints on MOT during the LGM from different lines of evidence (the noble gas record provided here, and refs 4 and 9). Just from this simple consideration it is obvious that the LGM ocean temperature pattern must have been different from today's. To account for this aspect we split the ocean box into three boxes representing AABW, NADW and all other waters (RES). We set the temperature, volume and salinity of AABW and NADW according to ref. 20 (AABW: −0.88 °C, 35% of total ocean volume, 34.641 PSS; NADW: 2.3 °C, 20% of total volume, 34.886 PSS) and set the RES ocean such that the averaged ocean corresponds to today's average conditions (3.53 °C, 1.34×10^{18} m^3, 34.72 PSS)[70]. In a first experiment we change the temperatures of the different volumes equally as long as AABW does not reach −2 °C. If this happens AABW temperature is set to −2 °C (non-freezing) and the remainder of the cooling is compensated by the other water masses to equal shares. This requires a lower LGM MOT of −0.2 °C owing to the nonlinearity of the solubility functions and gives a sense of how strong the effect of a changing temperature distribution can be on our MOT reconstruction.

The non-freezing AABW experiment described above follows a somewhat artificial path of the ocean temperature/volume distribution. A more realistic scenario is that AABW volume was larger in glacial times, similar to what ref. 22 describes. We use a scenario in which AABW during LGM was 40% bigger than it is today and shrank linearly over the course of the LGM–Holocene transition (17,900–11,550 yr BP) to the current situation found in ref. 20. We choose 40% because it roughly compensates the reduced AABW cooling/warming potential with its change in volume at the expense of the other (warmer) water masses. This more realistic (but still arbitrary) scenario halves the effect of a change in the temperature distribution on the LGM–Holocene MOT difference to −0.1 °C.

We use this three-ocean box model version including all elements and the AABW volume change scenario described so far for our MOT reconstructions shown in the main text. The analytical uncertainties and uncertainties of the sea-level change record are propagated to our MOT estimate, creating 3,000 Monte-Carlo MOT realizations for each data point. The same procedure is done using the two firn thermal gradient scenarios and undersaturation scenarios described earlier. This results in 12,000 MOT record realizations for each ratio and 36,000 MOT record realizations in total. Our best-estimate record is derived based on all these realizations, which provides an objective representation of all uncertainty elements discussed here. For our LGM–Holocene MOT change estimate (see averaging periods in Fig. 3) we also make use of all these realizations while we interpret the propagated measurement and the sea-level change uncertainties as of stochastic nature and treat them as normally distributed uncertainties. However, the uncertainty introduced by the Xe (and Kr) undersaturation effect we treat as non-stochastic because it represents equally likely scenarios. This source of uncertainty represents the largest contribution to the overall uncertainty and with this approach we find a LGM–Holocene MOT difference of 2.57 ± 0.24 °C.

In Extended Data Table 1 we list three more elements that are not included in our MOT records, but are discussed here for completeness. As described in ref. 22, the glacial ocean circulation might have been characterized by an approximately 1PSS saltier AABW cell owing to missing fresh water input from melting sea ice in the Southern Ocean. As the salt content can be assumed to be conserved in the ocean on these timescales, the additional salt in AABW has to be provided by NADW and RES. Owing to the salinity dependency of the solubility functions, such a salinity redistribution leads to different weights of the differently warm water masses in the MOT reconstruction. We tested this effect by a salinity anomaly of 1PSS applied to our AABW cell (compensated by NADW and RES by equal shares) and find a small effect of only −0.02 °C on the LGM MOT estimate.

Another aspect we test is the potential bias caused by a large floating ice shelf. Noble gases are basically only dissolving in the liquid phase of the ocean but the sea-level change record does not capture the corresponding liquid ocean volume change as opposed to ice that is stored on land. We assume an ice shelf with the extent of the modern winter sea ice around Antarctica and a thickness of 200 m. This seems gigantic, as we do not have any evidence that such a large ice shelf could have existed. The effect of such an ice shelf on the LGM MOT estimate would only be −0.1 °C and shows that this potential bias is also of minor relevance.

The last row in Extended Data Table 1 shows the effect of the applied 2% correction of the Xe solubility function compared to the case in which we do not apply this correction. Mass conservation of the noble gases in the model means that this temperature-independent change in the solubility function of Xe leads to a slight change in the MOT sensitivity of the ratios, including Xe (Xe/N_2 and Xe/Kr). The effect on the LGM MOT estimate, however, would only be 0.04 °C and 0.07 °C, respectively, showing that the results presented here are not much affected by this existing uncertainty in the Xe solubility. Kr is about a factor of two less soluble in sea water than Xe and the solubility function of Kr is better constrained[15] than is Xe. For these reasons, the effect on the LGM MOT estimate of the uncertainty in the Kr solubility function is much smaller than what is shown for Xe in Extended Data Table 1 and can therefore be neglected.

Scaling MOT to surface temperatures based on global climate models. MOTs are set by surface ocean temperatures, which in turn are related to global surface temperatures. The connection between surface and ocean interior temperature changes is, however, also dependent on the climatology (polar amplification, ocean circulations, location of deep water formation areas, and so on), which is different for glacial and interglacial periods. The constraints on the glacial climatology are fairly weak and the realization of such climatology within a climate model can be very different from model to model. Therefore, we use several independent climate models that provide climatology for glacial and interglacial conditions and calculate the scaling factors from MOT to ASST and GAST changes, respectively (see ΔASST/ΔMOT and ΔGAST/ΔMOT in Extended Data Table 2).

Such glacial–interglacial climate model experiments are part of the Paleoclimate Modelling Intercomparison Project (PMIP), which can be accessed openly via one of the Coupled Model Intercomparison Project (CMIP) data nodes. All results found in Extended Data Table 2 are based on model output from the PMIP3 project (ensemble: r1i1p1; see ref. 71 for more details about the CMIP5/PMIP3 experiments), with the exception of the Bern3D model results which were provided for this study. From the PMIP3 project results, we used the following variables from the LGM and the Pre-industrial Control experiments: (1) global averaged sea water potential temperature (thetaoga), (2) seawater potential temperature (thetao), and (3) near surface air temperature (tas). Where available, we averaged the thetaoga data to derive MOT. If only thetao was available (three-dimensional field) we averaged over the time dimension covered by the corresponding dataset (12 months) and then over the space dimension while weighting the cell values by the corresponding cell volumes. ASST was calculated by first filtering all surface cells in thetao that are covered by more than 50% with sea ice, followed by the same temporal and spatial averaging as done for MOT. Therefore, our ASST values represent the open ocean surface temperatures excluding the areas covered by sea ice, where the heat exchange with the atmosphere is negligible and the surface ocean temperature is set to freezing temperature of the corresponding water (dependent on salinity). GAST was calculated by averaging the tas fields (two-dimensional fields).

The results in Extended Data Table 2 show that the LGM–Holocene MOT difference varies strongly from model to model mainly owing to discrepancies in the LGM values. This shows that the models provide quite different climatologies in particular for the LGM conditions. Therefore the range of these model results can be interpreted according to how much different climatologies can affect the scaling factor between the globally averaged parameters calculated here. The ΔASST/ΔMOT scaling factor varies from 0.67 to 0.89 with an ensemble average of 0.80. The ΔGAST/ΔMOT scaling factor varies from 1.96 to 2.92 with an ensemble average of 2.50.

In general, the models underestimate the MOT difference between the LGM and the Holocene with an ensemble average of 1.60 °C and a range from 0.92 °C to 1.95 °C, which raises the question of whether the large spread of the scaling factors is correlated to the absolute LGM–Holocene MOT difference and, hence, may contain a bias. However, there is no correlation between the absolute LGM–Holocene MOT difference and the scaling factors, for which reason any possible bias in these scaling factors is believed to lie within the model spread.

Hypothesis behind the Younger Dryas MOT anomaly. As discussed in the main text, our MOT record shows a phase of outstanding strong and fast warming during the first half of the Younger Dryas (referred to as YD1). Here we discuss two possible underlying mechanisms.

One condition that might underlie the strong MOT warming/heat uptake during YD1 could be the strong insolation in high latitudes associated with the phase of high obliquity around YD1 (Fig. 3). In the latitudes where deep waters are formed, the local annual averaged heat flux was about 1.5 W m^{-2} higher than during the LGM. The additional heat flux could have led to an increased warming of surface waters near the deep-water formation areas during the summer seasons, which would have then been transported into the deep ocean during the winter seasons, when deep-water formation mainly occurs. The pattern of the YD1 warming, however, is not consistent with the gradual insolation change, requiring additional processes at work. For the period before the YD1 warming and its abrupt start, the change in AMOC state can provide such an explanation: before the YD1 the strong AMOC state pulls the warm waters towards the north, preventing warming of the deep (southerly ventilated) ocean. The collapse/weakening of the AMOC at the beginning of the YD1 stopped this northward heat pull and, thus, triggers the rapid YD1 warming. But for the end of the YD1 warming, which occurs considerably before the end of the Younger Dryas when the AMOC accelerates again, the AMOC can no longer explain the observation. Note that these orbital-driven heat flux changes are fairly small with regard to the baseline flux of

about 234 W m^{-2} (today). Hence, they might have been only of minor importance for the YD1 MOT anomaly.

Another hypothesis that could explain the MOT pattern during the Younger Dryas is that a cold, isolated water mass was ventilated during YD1. This water mass would have last been ventilated several millennia earlier, for example during the cold LGM, and only the push of the Younger Dryas onset (collapse of AMOC[30]) would have brought this cold water up to the surface to equilibrate. The end of YD1 would then mark the point in time when this water mass was fully ventilated and hence this scenario would be able to provide an explanation for the stalled warming before the AMOC acceleration. Such a drastic change in ocean ventilation could be explained with a switch from a glacial ocean circulation mode to a modern/interglacial mode as mentioned in the main text. Multiple lines of evidences suggest the existence of such different ocean circulation modes[22–25], and in the case of the shift from interglacial to glacial mode, the 'MIS 5-4 transition' at around 70 kyr BP has been suggested as such[24,25]. The YD1 could be the counterpart of the MIS 5-4 transition, providing a relatively sharp definition of the last glacial period from an ocean circulation perspective.

Data availability. All relevant data from the ice samples (noble gas elemental and isotope ratios) are provided as Supplementary Data; the corresponding reconstructed mean ocean temperatures are provided as Source Data for Figs 2 and 3 and Extended Data Figs 1 and 2.

Code availability. The ocean box model, including the Monte Carlo code (Matlab), is available 'as is' from the corresponding author on request. Details of the ocean box model can also be found in refs 10 and 11.

43. Severinghaus, J. P., Grachev, A., Luz, B. & Caillon, N. A method for precise measurement of argon 40/36 and krypton/argon ratios in trapped air in polar ice with applications to past firn thickness and abrupt climate change in Greenland and at Siple Dome, Antarctica. *Geochim. Cosmochim. Acta* **67,** 325–343 (2003).
44. Kobashi, T., Severinghaus, J. P. & Kawamura, K. Argon and nitrogen isotopes of trapped air in the GISP2 ice core during the Holocene epoch (0-11,500 B.P.): Methodology and implications for gas loss processes. *Geochim. Cosmochim. Acta* **72,** 4675–4686 (2008).
45. Lüthi, D. *et al.* CO_2 and O_2/N_2 variations in and just below the bubble-clathrate transformation zone of Antarctic ice cores. *Earth Planet. Sci. Lett.* **297,** 226–233 (2010).
46. Neff, P. A review of the brittle ice zone in polar ice cores. *Ann. Glaciol.* **55,** 72–82 (2014).
47. Taylor, K. C. WAIS Divide Ice Core Project: end of season field report 2008/2009. http://www.waisdivide.unh.edu/docs/EOS-Field-Reports_2008-2009.pdf (2009).
48. Alley, R. B. WAIS Divide Ice Core Project: end of season field report 2007/2008. http://www.waisdivide.unh.edu/docs/EOS-Field-Reports_2007-2008.pdf (2008).
49. Severinghaus, J. P., Beaudette, R., Headly, M. A., Taylor, K. & Brook, E. J. Oxygen-18 of O_2 records the impact of abrupt climate change on the terrestrial biosphere. *Science* **324,** 1431–1434 (2009).
50. Souney, J. M. *et al.* Core handling and processing for the WAIS Divide ice-core project. *Ann. Glaciol.* **55,** 15–26 (2014).
51. Bereiter, B., Schwander, J., Lüthi, D. & Stocker, T. F. Change in CO_2 concentration and O_2/N_2 ratio in ice cores due to molecular diffusion. *Geophys. Res. Lett.* **36,** (2009).
52. Schmitt, J. *et al.* Carbon isotope constraints on the deglacial CO_2 rise from ice cores. *Science* **336,** 711–714 (2012).
53. Wanninkhof, R. Relationship between wind speed and gas exchange over the ocean revisited. *Limnol. Oceanogr. Methods* **12,** 351–362 (2014).
54. Keeling, R. F. *et al.* Measurement of changes in atmospheric Ar/N_2 ratio using a rapid-switching, single-capillary mass spectrometer system. *Tellus B* **56,** 322–338 (2004).
55. Viglione, G. A. & Thompson, A. F. Lagrangian pathways of upwelling in the Southern Ocean. *J. Geophys. Res. Oceans* **121,** 6295–6309 (2016).
56. Spahni, R. *et al.* The attenuation of fast atmospheric CH_4 variations recorded in polar ice cores. *Geophys. Res. Lett.* **30,** (2003).
57. Snow, K., Sloyan, B. M., Rintoul, S. R., Hogg, A. M. & Downes, S. M. Controls on circulation, cross-shelf exchange, and dense water formation in an Antarctic polynya. *Geophys. Res. Lett.* **43,** 7089–7096 (2016).
58. Schwander, J. Gas diffusion in firn. In *Chemical Exchange Between the Atmosphere and Polar Snow* (eds Wolff, E. W. & Bales, R. C.) *NATO ASI Series I: Global Environmental Change* Vol. 43 (Springer, 1996).
59. Kawamura, K. *et al.* Kinetic fractionation of gases by deep air convection in polar firn. *Atmos. Chem. Phys. Discuss.* **13,** 7021–7059 (2013).
60. Headly, M. A. *Krypton and xenon in air trapped in polar ice cores: paleo-atmospheric measurements for estimating past mean ocean temperature and summer snowmelt frequency*. PhD thesis, Univ. California, San Diego (Scripps Institution of Oceanography, 2008).
61. Buizert, C. & Severinghaus, J. P. Dispersion in deep polar firn driven by synoptic-scale surface pressure variability. *Cryosphere* **10,** 2099–2111 (2016).
62. Hamme, R. C. & Emerson, S. R. The solubility of neon, nitrogen and argon in distilled water and seawater. *Deep. Sea Res. I* **51,** 1517–1528 (2004).
63. Weiss, R. F. & Kyser, T. K. Solubility of krypton in water and seawater. *J. Chem. Thermodyn.* **23,** 69–72 (1978).
64. Wood, D. & Caputi, R. Solubilities of Kr and Xe in fresh and sea water. (US Naval Radiological Defense Laboratory, 1966).
65. Schlatter, T. W. *Atmospheric Composition and Vertical Structure* eae31MS, http://citeseerx.ist.psu.edu/viewdoc/download?doi=10.1.1.532.2310&rep=rep1&type=pdf (NOAA Earth Systems Research Laboratory, 2009).
66. Alduchov, O. a. & Eskridge, R. E. Improved Magnus form approximation of saturation vapor pressure. *J. Appl. Meteorol.* **35,** 601–609 (1996).
67. He, F. *et al.* Simulating global and local surface temperature changes due to Holocene anthropogenic land cover change. *Geophys. Res. Lett.* **41,** 623–631 (2014).
68. Allan, R. & Ansell, T. A new globally complete monthly historical gridded mean sea level pressure dataset (HadSLP2): 1850-2004. *J. Clim.* **19,** 5816–5842 (2006).
69. Jiang, D. & Lang, X. Last Glacial Maximum East Asian monsoon: results of PMIP simulations. *J. Clim.* **23,** 5030–5038 (2010).
70. Sarmiento, J. L. & Gruber, N. *Ocean Biogeochemical Dynamics* (Princeton Univ. Press, 2006).
71. Schmidt, G. A. *et al.* Using palaeo-climate comparisons to constrain future projections in CMIP5. *Clim. Past* **10,** 221–250 (2014).

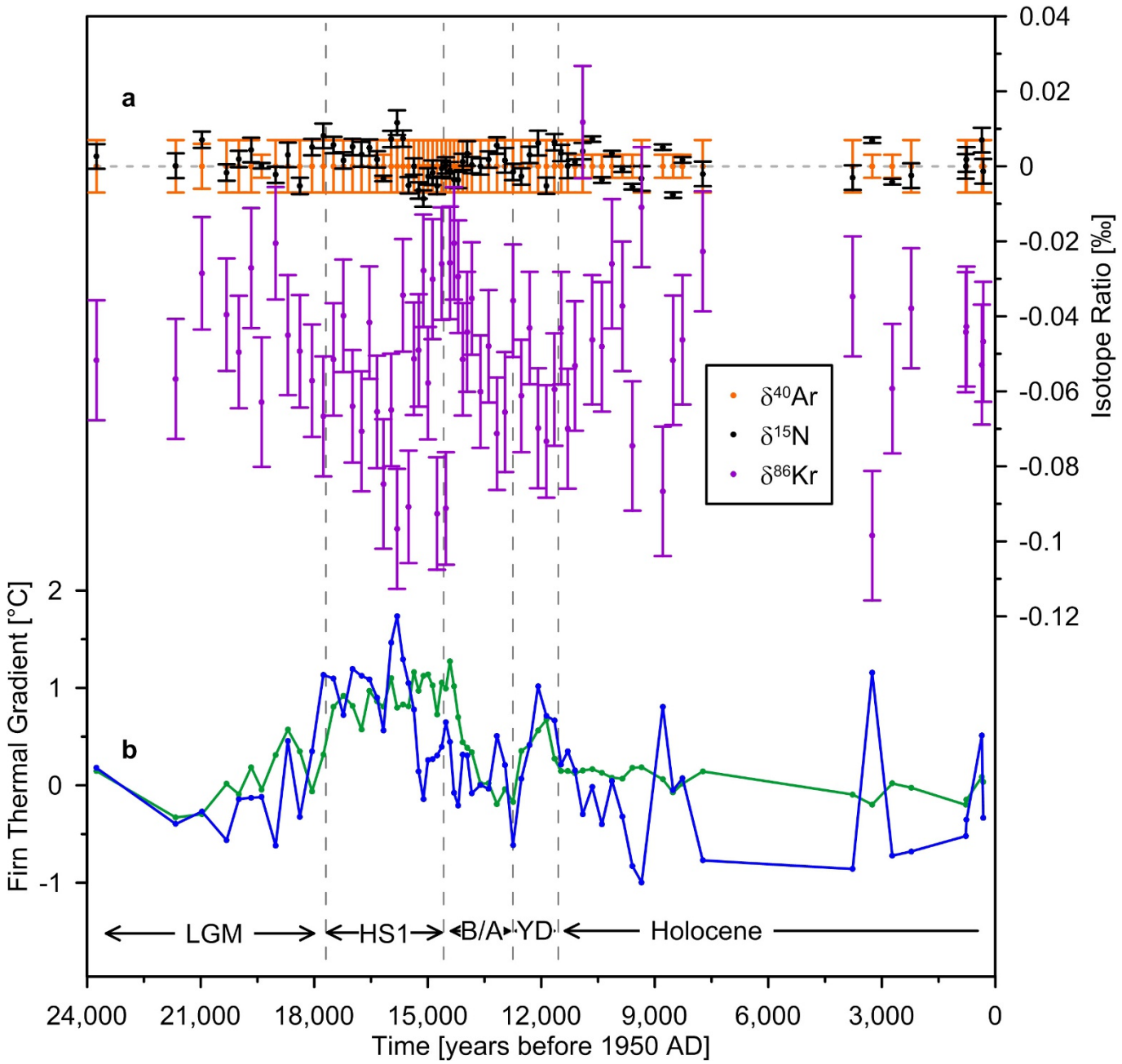

Extended Data Figure 1 | Elements related to the gravitational and thermal correction applied to the ice core data. a, Residual of the isotope data after correction for gravitational enrichment in the firn based on δ^{40}Ar (orange) and modelled firn thermal gradients (**b**, green[36]). In contrast to δ^{15}N (black), δ^{86}Kr (purple) clearly deviates from the zero line by −56 per meg on average, showing that our correction factors for δ^{86}Kr are over-estimated (δ^{40}Ar is zero by definition because we use this data for the correction). Error bars represent the 1σ analytical uncertainty of our method based on repeated measurements of modern air samples[10]. **b**, The two independent WAIS Divide ice core site firn thermal gradient scenarios used in this study. The blue trace represents the scenario derived from our isotope data for δ^{15}N, δ^{40}Ar and δ^{86}Kr, while first we corrected δ^{86}Kr by the offset seen in **a**. The green trace represents the model-based scenario and originates from ref. 36.

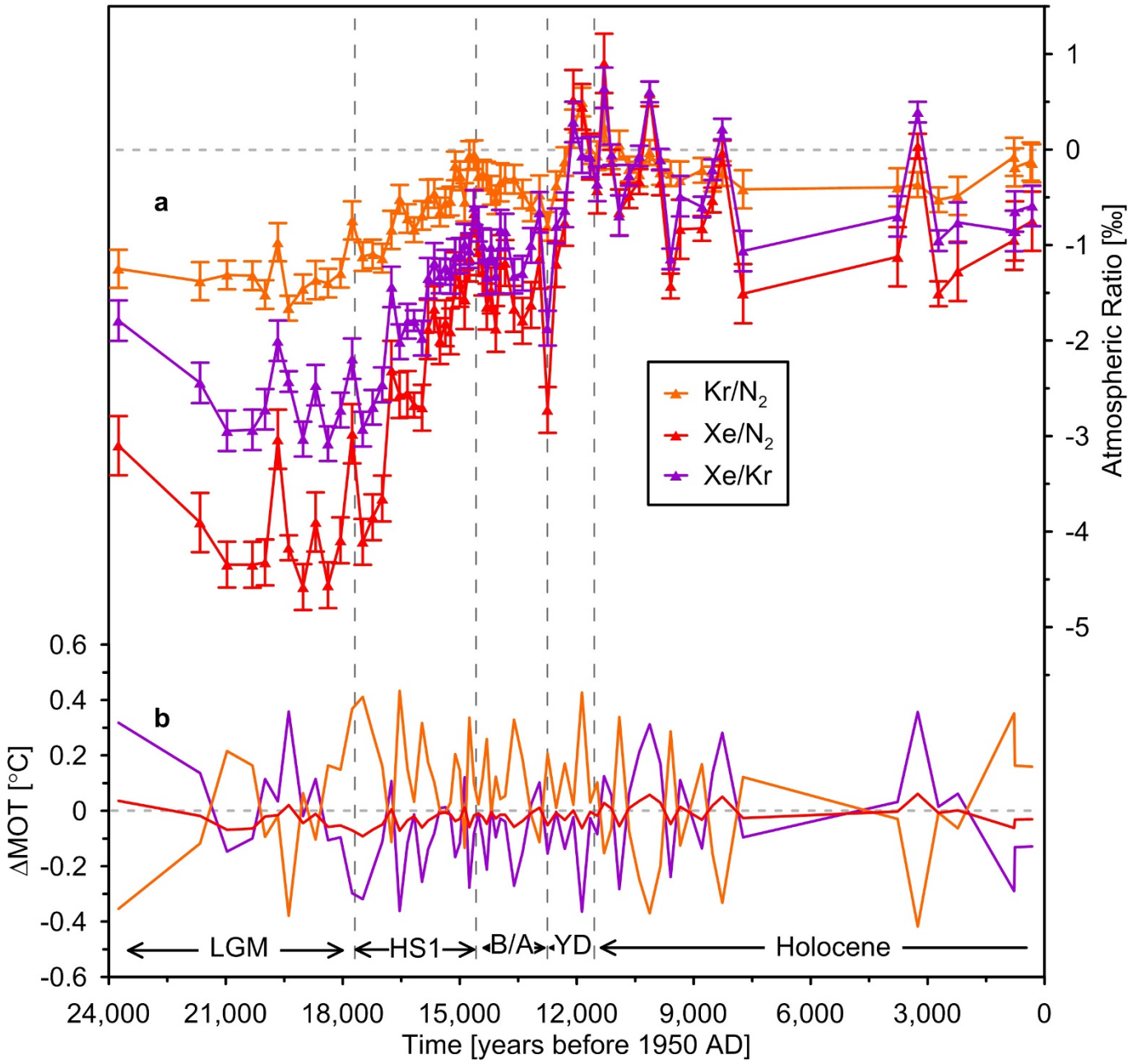

Extended Data Figure 2 | Raw atmospheric noble gas elemental ratios and relative differences between individual MOT records. **a**, Reconstructed atmospheric elemental ratios (orange, $\delta Kr/N_2$; red, $\delta Xe/N_2$; purple, $\delta Xe/Kr$) using $\delta^{40}Ar$ to correct for gravitational enrichment in the firn, and using the firn thermal gradient scenario based on our isotope data (see Extended Data Fig. 1) to correct for thermal fractionation. The error bars are 1σ. **b**, Differences in MOT derived from each of the three individual gas ratios relative to the best-estimate (Mix) data (compare with Fig. 1; orange, Kr/N_2 versus Mix; red, Xe/N_2 versus Mix; purple, Xe/Kr versus Mix).

Extended Data Table 1 | Effects of box-model elements on the LGM–Holocene MOT difference

Model element	LGM values relative to Holocene	Element specific effect on LGM-Holocene MOT difference
Noble Gases	-1.2‰ (Kr/N_2) -2.5‰ (Xe/Kr) -3.7‰ (Xe/N_2)	-1.8°C -2.2°C -2.1°C
SLC - sum of all effects	-132 m	-0.5°C
SLC - volume	-3.5%	-0.6°C
SLC - salinity	+3.5%	-0.2°C
SLC - SSP	+1.5%	+0.3°C
SSP related to H_2O content of atmosphere	-0.04%	<-0.02°C
SSP in high latitudes	-3% (constant offset)	-0.05°C
Kr and Xe saturation state	+50%	<+0.02°C (Kr/N_2) +0.3°C (Xe/N_2) +0.4°C (Xe/Kr)
Non-freezing of AABW	-	-0.2°C
AABW volume	+40%	+0.1°C
Total LGM-Holocene MOT change		2.57 +/- 0.24°C
AABW salinity anomaly*	+1 PSS	-0.02°C
Floating ice shelf volume*	+2.6e15 m^3	-0.1°C
Xe solubility function correction*	+2% (constant offset)	+0.04°C (Xe/N_2) +0.07°C (Xe/Kr)

Sea-level change (SLC) effects are most important, but other effects are also listed. SSP, sea surface pressure.
*These elements are not considered in our MOT record (see Methods).

Extended Data Table 2 | Simulated ocean and surface temperatures

	Bern3D	CNRM-C5	CCSM4	FGOALS	MIROC	MPI	MRI	**Ensemble Mean**
MOT PiC	4.02	4.24	3.21*	3.68	4.13	4.94#	4.24	**4.07**
GAST PiC	15.28#	13.20	13.33	12.43*	13.60	13.64	13.59	**13.58**
ASST PiC	19.51	18.94	19.75#	18.84	18.75	18.50*	19.59	**19.13**
MOT LGM	2.32	3.32#	1.26*	2.59	2.42	3.03	2.31	**2.46**
GAST LGM	11.94#	10.57	8.42	7.70*	8.60	9.23	8.91	**9.34**
ASST LGM	18.05	18.16	18.28#	16.81*	17.22	17.22	17.96	**17.67**
ΔASST/ΔMOT	0.86	0.85	0.75	(1.86#)	0.89	0.67*	0.84	**0.80**
ΔGAST/ΔMOT	1.96*	2.86	2.52	(4.34#)	2.92	2.31	2.42	**2.50**

PiC, Pre-industrial Control. MOT and ASST are calculated by averaging the potential temperature fields in time and space of the corresponding experiments (see main text), while for ASST the sea-ice-covered area was excluded. GAST is calculated by similar averaging of the corresponding air temperature fields. The values denoted with # and * mark the highest and lowest value of the corresponding row, respectively. The 'Ensemble Mean' column shows the average of the seven models Bern3D, CNRM-C5, CCSM4, FGOALS, MIROC, MPI and MRI summarized in this table. The ΔGAST/ΔMOT and ΔASST/ΔMOT scaling factors of the FGOALS model are rejected because the former would suggest an unrealistically cold GAST for the LGM of 11 °C below today's and because both values are outliers with respect to the corresponding values of the other models. Detailed information about the individual models and the output data we used can be found on any publicly accessible data server node (such as https://esgf-data.dkrz.de) of the CMIP project.